(Received 3 April 2024, Accepted 22 May 2024, Scheduled 18 June 2024)

Active Disturbance Rejection Control Strategy for a Novel Wide-Rotor Bearingless Switched Reluctance Motor

Yonghong Huang*, Meng Sun, Ye Yuan, Fan Yang, and Xinyue He

School of Electrical and Information Engineering, Jiangsu University, Zhenjiang 212013, China

ABSTRACT: A novel three-unit 8/4 wide-rotor bearingless switched reluctance motor has been designed to address the challenges of strong coupling and control difficulties between torque and suspension force in traditional bearingless switched reluctance motors. This motor features independent torque flux paths and suspension flux paths, allowing for separate control of torque and suspension force similar to traditional switched reluctance motors and active magnetic bearings. To tackle issues such as torque ripple, suspension force ripple, and reduced system robustness caused by external disturbances during operation, a torque sharing function and a suspension current PWM control strategy based on active disturbance rejection technology have been proposed. Firstly, mathematical models for the torque and suspension force of the three-unit 8/4 wide-rotor bearingless switched reluctance motor were established using Ansys simulation data and the Maxwell stress method. Subsequently, a torque sharing function and a suspension current PWM control system were developed based on these mathematical models. The endpoint of the commutation overlap zone was set at the maximum value of the phase inductance to eliminate the weak coupling effect of torque current on suspension force. Finally, active disturbance rejection control technology was introduced to compare its performance with that of traditional PID controllers in suppressing interference. Simulation results demonstrate that the proposed method ensures decoupling switching between each phase's motor torque and its associated suspension while enhancing anti-interference performance.

1. INTRODUCTION

Bearingless Switched Reluctance Motor (BSRM) is characterized by its simple structure, high mechanical strength, low suspension loss of Active Magnetic Bearing (AMB), and simple control. It has been widely utilized in aerospace, rail transit, and other fields. The concept of BSRM was initially proposed by Japanese scholars Takemoto et al. [1]. They adopted a double-winding structure and added additional suspension windings to the traditional SRM to achieve rotation and suspension of the rotor. However, the double-winding structure increased costs and motor design complexity, leading to the development of single-winding BSRM. The research on 12/8, 8/10, 12/4, and 8/6 single-winding BSRMs has been conducted by NASA in the United States, Jiangsu University in China, Nanjing University of Aeronautics and Astronautics, Beijing University of Aeronautics and Astronautics among other universities [2–6], yielding certain results. Nevertheless, the paths of torque flux and suspension flux in traditional bearingless switched reluctance motors coincide, with both torque and suspension force being generated by the magnetic pull between the tooth electrodes of the fixed rotor, overlapping each other. Consequently, there is inevitable mutual influence during control, resulting in control coupling. To achieve independent control of torque and suspension force, it is necessary to employ decoupling control algorithms such as neural network inverse system method or least square method. However, this increases the complexity of control system design and reduces online operation speed. To address these issues while considering the balance of axial distribution of torque and suspension force, a three-unit 8/4 wide-rotor BSRM is designed in this paper. The rotor pole arc is twice that of the stator pole arc; the inductance rising area generates torque, and the inductance flat top area produces suspension force. Continuous torque and suspension force can be generated through coordination among front, middle, and back three motor units.

The BSRM control system primarily regulates torque and suspension force. In [7], the average suspension force and average torque control are proposed, with both torque windings and suspension windings adopting square wave control. While this strategy can avoid complex winding current calculations during high-speed motor operation, it is only suitable for situations with low suspension accuracy. Nonlinear control methods, such as sliding mode control, adaptive control, and neural network algorithms, have been widely utilized in BSRM control systems. Based on finite element analysis and artificial neural network method, [8] established a BSRM mathematical model based on nonlinear magnetic circuit and proposed a direct suspension force control strategy. However, the system algorithm is complex and not easily implemented online. In [9], a zonal control of BSRM torque and suspension force was proposed. Traditional current chopper control was adopted for the torque part, while a similar magnetic bearing control method was used for the suspension force to design the overall control system. Nevertheless, the influence of external disturbances on the motor's operating state was not considered.

* Corresponding author: Yonghong Huang (hyh@ujs.edu.cn).

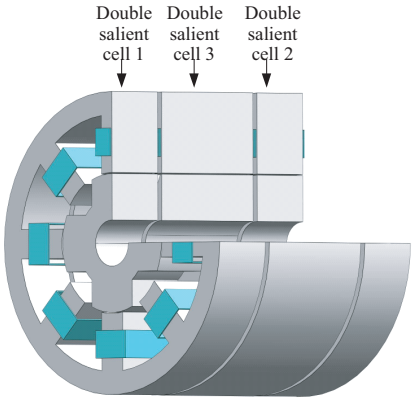

FIGURE 1. Motor overall structure profile.

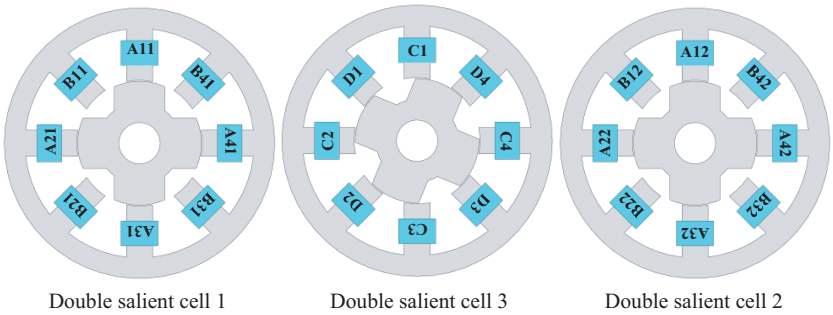

FIGURE 2. Schematic diagram of the three-unit structure.

Although the traditional proportion integration differentiation (PID) controller has the advantages of an independent mathematical model of the controlled object and few tuning parameters, it lacks sufficient ability to restrain external disturbances. Building on the PID Control concept, Han [10] proposed active disturbance rejection control (ADRC). The core idea is to reduce all uncertainties, including internal parameter perturbations and external perturbations, to total perturbations and expand them into system state variables. The extended state observer is utilized to estimate and compensate for the total perturbations in real time, ultimately simplifying the controlled objects into series integrators. ADRC has been widely applied in motor control, power systems, and other fields due to its exceptional disturbance suppression capability. However, ADRC employs a nonlinear function with numerous parameters that are difficult to set, making its stability challenging to analyze. GAO [11] introduced linear active disturbance rejection control (LADRC), which uniformly configures the parameters of the extended state observer and controller based on their respective bandwidths. This greatly reduces the difficulty of parameter setting while ensuring system stability.

Based on LADRC technology, this paper presents the construction of a three-unit 8/4 wide-rotor BSRM control system. The Torque Sharing Function (TSF) control strategy is employed in the torque section to mitigate torque ripple, while the suspension part utilizes Suspension Current Pulse Width Modulation Control (SCPWM) to enhance rotor suspension accuracy. Through simulation, it is demonstrated that the LADRC controller outperforms the traditional PID controller in disturbance suppression.

2. STRUCTURE AND MATHEMATICAL MODEL OF 8/4 WIDE-ROTOR BSRM

2.1. Ontology Structure and Working Principle

The BSRM structure of the three-unit 8/4 wide-rotor is illustrated in Figures 1 and 2. The motor consists of three 8/4 double salient pole units, with the stator of the three double salient pole units being precisely aligned axially. The rotor of the double salient pole unit 3 and the rotor of the double salient pole units 1 and 2 have a spatial dislocation of 22.5°. There are four phases in the motor, with phase A and B windings distributed on double salient pole units 1 and 2, while phase C and D windings are distributed on double salient pole unit 3. The windings A11, A21, A31, A41, B11, B21, B31, B41 of double salient unit 1 are connected in series with the windings A12, A22, A32, A42, B12, B22, B32, B42 of double salient unit 2 respectively to form phase A and phase B. The windings C1, C2, C3, and C4 of double salient unit 2 form phase C. D1, D2, D3, and D4 form phase D. Each phase has four sets of windings which are independently controlled.

Consistent with traditional SRM, the three-unit 8/4 wide-rotor BSRM also adheres to the principle of "minimum reluctance", and its winding inductance curve is depicted in Figure 3. Taking phase A as an example, when the inductor is positioned in the rising region, relatively equal excitation of phase A generates torque; when the inductor is located in the upper flat top region, asymmetric excitation of phase A generates suspension force; when the inductor is situated in the falling region and lower flat top region, suspension force is generated. There is no current flowing through phase A winding. The exciting current passes through phases A→C→B→D sequentially. During rotor rotation, both torque and suspension can be independently adjusted through partition control utilizing the motor's special structural characteristics. The working state of the winding within one rotor angle period is presented in Table 1.

TABLE 1. Three unit 8/4 wide-rotor BSRM working status.

θ (deg)	0 ∼ 22.5	22.5 ∼ 45	45 ∼ 67.5	67.5 ∼ 90
A	torque	suspension	/	/
B	/	/	torque	suspension
C	/	torque	suspension	/
D	suspension	/	/	torque

It is evident from Table 1 that the two phases are responsible for generating torque and suspension force respectively at any given time. Additionally, as shown in Figure 2, the three-unit structure distribution illustrates that the torque flux and suspen-

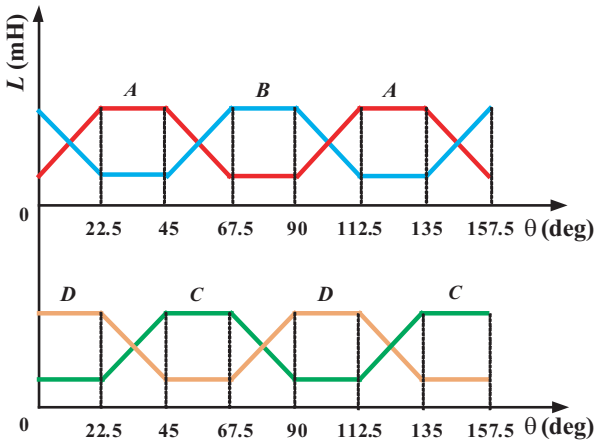

FIGURE 3. Four-phase inductance curve.

sion flux circulate independently in different double salient pole elements without interfering with each other. This indicates that the magnetic flux path is independent. To control torque, it is only necessary to adjust the magnitude of the winding excitation current in the double salient pole unit responsible for generating torque. Similarly, controlling suspension force only requires adjusting the size of the suspension excitation current in the double salient pole unit responsible for providing suspension force. As a result, independent control of both torque and suspension force can be achieved [12].

Based on the winding connection mode of the three-unit 8/4 wide-rotor BSRM and the analysis presented in Table 1, it is evident that during a rotor Angle period, torque is generated by double salient pole elements 1 and 2 located at the front and rear, respectively, when the rotor position Angle ranges from 0° to 22.5° and from 45° to 67.5°. Additionally, suspension force is produced by double salient pole element 3 situated in the middle. Conversely, when the rotor position Angle falls within the range of 22.5° to 45° and from 67.5° to 90°, torque is generated by double salient pole unit 3 while suspension force is produced by double salient pole units 1 and 2. Therefore, this three-unit structure ensures a balanced axial distribution of both torque and suspension force during operation.

2.2. Mathematical Model

The mathematical model of the torque system is established using the table lookup method. The winding phase voltage balance equation is as follows:

$$U = Ri + \frac{d\psi}{dt} = Ri + L\frac{di}{dt} + i\frac{dL}{dt} \tag{1}$$

where U is the winding terminal voltage, R the phase resistance, i the phase current, ψ the phase winding flux, and L the phase winding inductance.

Inductance L and torque T are both nonlinear functions of current i and rotor position angle θ. Therefore, the data curves for torque and inductance with respect to current and rotor position angle are obtained through finite element simulation. The inductance table look-up module and torque table look-up module are built from the finite element simulation data in Figure 4 and Figure 5, respectively.

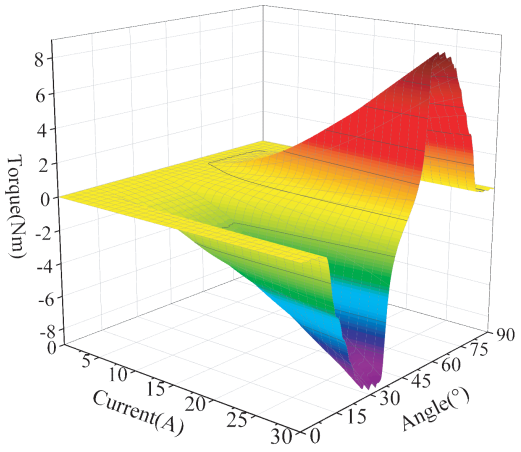

FIGURE 4. Torque-Angle-Current curve.

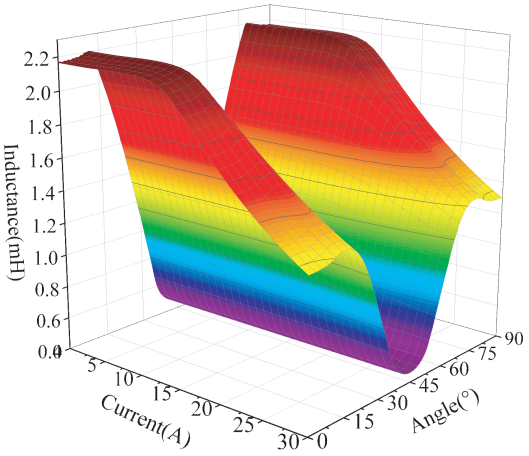

FIGURE 5. Inductance- Angle-Current curve.

The torque excitation current is calculated according to Equation (1) and the inductance table module, and the torque is output through the excitation current and the rotor position through the torque table module.

As illustrated in Figure 6, the suspension force of the three-unit 8/4 wide-rotor BSRM is divided into x and y directions (the directions indicated by the coordinate axes in the figure are all positive). Since the principle of the suspension force in x and y directions is identical, the mathematical model is derived using the x direction as an example. The suspension force is generated by both the bias magnetic field and control magnetic field. The bias magnetic field is produced by continuous torque current, while the control magnetic field is generated by suspension control current. The equivalent magnetic circuit of the bias magnetic field and control magnetic field can be seen in Figure 7 and Figure 8, respectively, where N is the number of winding turns on each stator tooth, R the air gap reluctance, i_m the bias current, i_c the control current, φ the bias flux, and φ_c the control flux.

If the motor rotor produces a displacement eccentricity of magnitude x_0 in the x-direction, then the bias fluxes of x_+ and

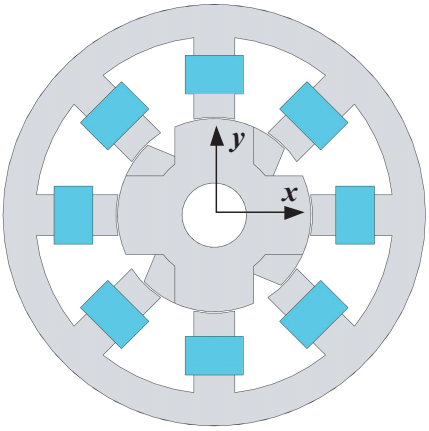

FIGURE 6. Diagram of levitation force direction

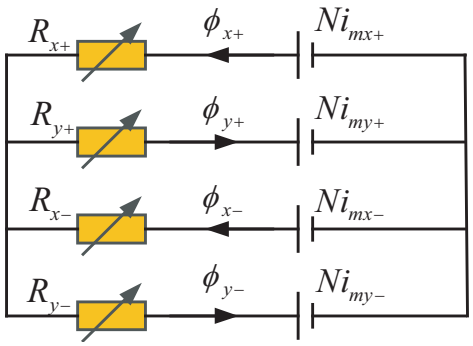

FIGURE 7. Bias field equivalent magnetic circuit.

x_- directions are:

$$\begin{cases} \phi_{mx+} = \frac{Ni_m}{R_{x+}} = \frac{Ni_m}{\frac{g+x_0}{\mu_0 S}} = \frac{\mu_0 S N i_m}{g+x_0} \\ \phi_{mx-} = \frac{Ni_m}{R_{x-}} = \frac{Ni_m}{\frac{g-x_0}{\mu_0 S}} = \frac{\mu_0 S N i_m}{g-x_0} \end{cases} \tag{2}$$

where μ_0 is the vacuum permeability, g the air gap length, and S the stator pole arc area.

The control flux generated by the suspension control current is:

$$\phi_{cx+} = \phi_{cx-} = \frac{2Ni_{cx}}{R_{x+} + R_{x-}} = \frac{\mu_0 S N i_c}{g} \tag{3}$$

Then the total magnetic fluxes in the x_+ direction and the x_- directions are:

$$\begin{cases} \phi_{x+} = \phi_{mx+} + \phi_{cx+} \\ \phi_{x-} = \phi_{mx-} - \phi_{cx-} \end{cases} \tag{4}$$

According to Maxwell stress method [13], the suspension force generated at x degrees of freedom is:

$$F = \frac{\phi_{x+}^2}{2\mu_0 S} - \frac{\phi_{x-}^2}{2\mu_0 S} \tag{5}$$

By substituting Equations (2) $\sim$ (4) into Equation (5), the mathematical model of the three-element 8/4 wide rotor BSRM suspension system is calculated as follows:

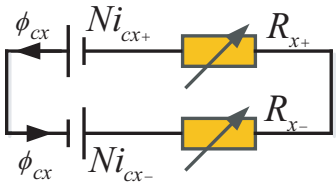

FIGURE 8. Control field equivalent magnetic circuit.

$$F = \frac{2\mu_0 S N^2 g i_m}{g^2 - x_0^2} \left(\frac{i}{g} - \frac{x_0 i_m}{g^2 - x_0^2} \right) \tag{6}$$

By linearizing the rotor balance position and ignoring infinitely small quantities above the second order, we can obtain:

$$F = k_i i_c + k_x x_0 \tag{7}$$

where k_i is the current stiffness coefficient, and k_x is the displacement stiffness coefficient, both of which can be expressed by the motor structure parameters and winding current.

$$\begin{cases} k_i = \frac{2\mu_0 S N^2 i_m}{g^2} \\ k_x = -\frac{2\mu_0 S^2 N^2 i_m^2}{g^3} \end{cases} \tag{8}$$

Based on the operational principle of the three-unit 8/4 wide-rotor BSRM and the analysis of Equations (7) and (8), it is evident that although the torque flux and suspension flux paths of the motor do not coexist simultaneously within the body structure, and both torque and suspension force can be controlled independently, there is a continuous decline in torque current i_m when each phase switches from the torque phase to the suspension phase. The current stiffness coefficient and displacement stiffness coefficient also continue to change. In order to generate a stable suspension force, the suspension control current needs to be calculated in reverse according to the changing stiffness coefficient. The above is the weak coupling effect of torque current on the suspension system.

3. TSF AND SCPWM CONTROL STRATEGY

The body structure of the three-unit 8/4 wide-rotor BSRM is unique. According to the analysis of its operation principle, the torque and suspension force are generated by different motor units simultaneously, allowing for independent control similar to traditional SRM and AMB systems. However, the use of switching power supply and a double salient pole structure results in significant torque and suspension force pulsations. In order to effectively reduce these pulsations, a TSF control strategy is adopted for the torque part, and a PWM control strategy is adopted for the suspension part.

3.1. TSF Control Strategy

The torque output of the three-unit 8/4 wide-rotor BSRM is divided into single-phase on-zone and commutation overlap zone. In the single-phase on-zone, each phase outputs torque separately, while in the commutation overlap zone, the demagnetization phase and excitation phase jointly output torque. The

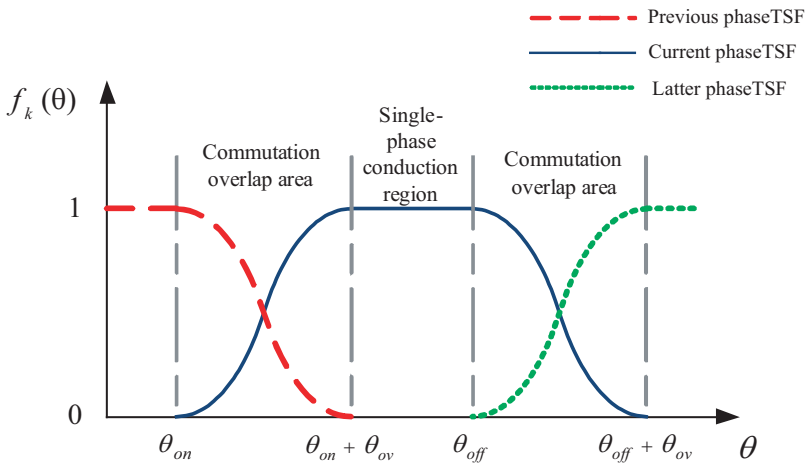

FIGURE 9. TSF curve.

core control idea of TSF is to allocate the corresponding given torque to each phase in both zones based on a predesigned function. The power circuit driven by PWM modulation ensures that the actual torque tracks the given value, thus ensuring stable torque output [14]. The specific control process involves several modules: proportional-integral (PI) controller calculates the total reference torque based on the error between the given speed and actual speed. Torque distribution module allocates the given torque to each phase according to reference torque and rotor position. Torque lookup module outputs actual torque for each phase based on rotor position and phase current. PWM modulation module calculates error between reference and actual torques for each phase, then combined with set carrier output corresponding switching signal controls power switch tube to adjust torque. Overall, these processes ensure precise control over the allocation of torque in different operating zones of BSRM, contributing to stable performance as required in academic research papers.

Figure 9 illustrates the TSF curve, which is divided into two zones: the commutation overlap zone and single-phase on-pass zone. In the single-phase on-pass zone, the function value is consistently 1. In the commutation overlap zone, both the demagnetization phase and excitation phase functions change according to specific rules. The sum of function values for each phase at any given time is always 1, satisfying the following condition

$$\begin{cases} \sum_{k=1}^{n} f_k(\theta) = 1 \\ 0 \le f_k(\theta) \le 1 \end{cases} \tag{9}$$

where n is the number of motor phases, and $f_k(\theta)$ is the torque sharing function value of the k phase.

The common TSF expression is as follows:

$$f_k(\theta) = \begin{cases} 0 & 0 \le \theta < \theta_{on} \\ f_{rise}(\theta) & \theta_{on} \le \theta < \theta_{on} + \theta_{ov} \\ 1 & \theta_{on} + \theta_{ov} \le \theta < \theta_{off} \\ f_{fall}(\theta) & \theta_{off} \le \theta < \theta_{off} + \theta_{ov} \\ 0 & \theta_{off} + \theta_{ov} \le \theta \le \tau \end{cases} \tag{10}$$

where f_{rise} is the excitation phase TSF; f_{fall} is the demagnetization phase TSF; θ_{on}, θ_{off}, and θ_{ov} are the opening angle, turn-off angle, and commutation overlap angle, respectively; and τ is the rotor angle period.

A well-designed function form is essential for the motor control system. Based on the different function curves of commutation overlap area shown in Figure 10, commonly used functions are mainly categorized into four types: linear, sinusoidal, exponential, and cubic ones.

Combined with the research background, the sinusoidal TSF with a wider speed range and lower copper consumption was ultimately chosen [15].

The torque ripple of the switched reluctance motor is more pronounced in the two-phase commutation zone. As shown in Figure 9, the TSF control strategy allocates corresponding torque to the excitation phase and demagnetization phase respectively in the commutation zone, and the demagnetization phase torque drops to 0 at the end of the commutation overlap zone. The excitation sequence of the three-element 8/4 wide rotor BSRM is A→C→B→D. The commutation process of A and C is used as an example. As shown in Figure 11, interval I is the commutation overlap area of A and C, and interval II is the single-phase on-off area of C. When the motor rotates to the starting point of interval I, phase A begins to be the demagnetization phase, and phase C is turned on as the excitation phase. The given torque of phase A begins to decline according to the sine law, and the inductance change rate of phase A is positive and constant before the maximum inductance value. Therefore, under the action of the inner loop torque error PWM modulation module, the A-phase current will continue to decrease until the rotor rotates to the end of interval I (the maximum A-phase inductance); the phase commutation process ends; the A-phase torque current drops to 0; and the A-phase inductance then enters the upper flat top region as A suspended phase, at which time the suspension force is only generated by the suspension current in the radial relative stator winding. The weak coupling effect of the torque current on the suspension system is eliminated because it is independent of the torque current continuity.

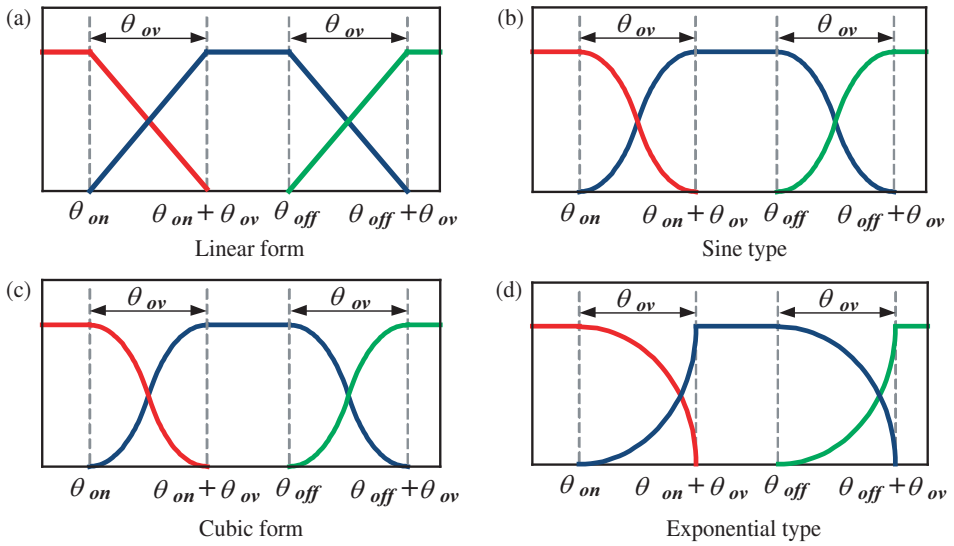

FIGURE 10. TSF classification.

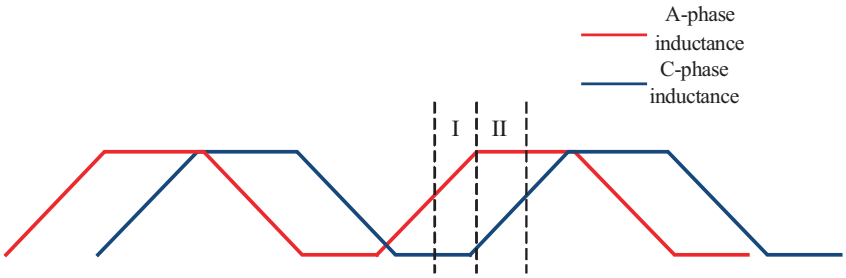

FIGURE 11. The configuration of the end point of commutation overlap area.

3.2. Suspension Current PWM Control Strategy

The suspension force is primarily generated by the radial magnetic pull resulting from the different suspension currents in the radial relative to the stator windings. In contrast to permanent magnet biased magnetic bearings, the three-unit 8/4 wide-rotor BSRM body structure does not rely on a permanent magnet to provide a bias magnetic field. Therefore, the bias current must be calculated based on extreme working conditions, as illustrated in Figure 11. Taking into account the requirement for the motor to output a maximum suspension force of 100 N under heavy load, a final bias current of 4 A is determined through simulation and analysis with an appropriate margin.

The core control idea of the suspension current PWM control strategy is to adjust the radial relative suspension winding current by superposition and cancellation of the control current and bias current, respectively, in order to generate unbalanced magnetic pull. Taking x degrees of freedom as an example, the specific control process is as follows: The displacement sensor detects the rotor displacement in real time. The PID controller outputs the error between the actual rotor displacement and the given displacement, which then determines the given suspension current of the radial relative suspension winding after calculating the control current and bias current. The inner loop PI controller generates an error between the actual current detected by the current sensor and its given value. The driving signal of the output power converter adjusts with PWM triangle carrier to ensure stable output of suspension force. Control processes for other degrees of freedom are similar to those described above.

In summary, Figure 13 illustrates the three-unit 8/4 wide-rotor BSRM control system.

4. TORQUE AND SUSPENSION FORCE ADRC CONTROLLER DESIGN

The operation of the motor is often affected by internal parameter perturbation and external disturbance. The traditional PID controller has poor anti-disturbance performance, leading to a deterioration in control performance. In order to address this issue, Active Disturbance Rejection Control (ADRC) technology is introduced. LADRC controller is used to replace the rotational speed outer loop PI controller and displacement outer loop PID controller in Figure 12 to improve the anti-disturbance performance of the control system.

4.1. Basic Structure of ADRC

Taking the 2nd-order ADRC as an example, as illustrated in Figure 14, the Linear ADRC comprises three components: Linear Tracking Differentiator (LTD), Linear State Error Feedback (LSEF), and Linear Extended State Observer (LESO).

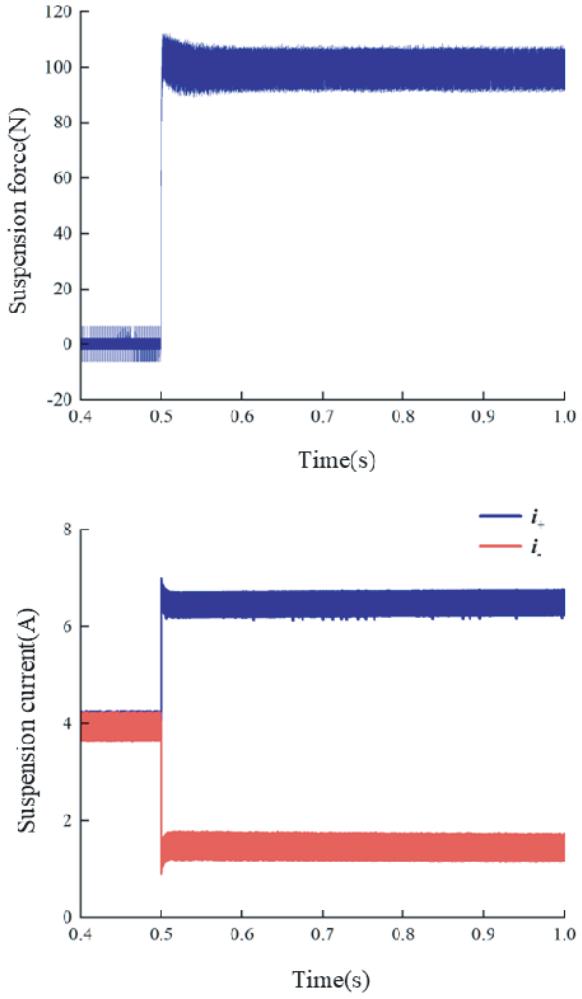

FIGURE 12. Bias current verification.

The purpose of LTD is to rapidly track the input reference signal and the differential of the output reference in order to complete the transition process. This effectively resolves the conflict between the speed and overshoot of traditional PID controllers [9]. The core component LESO can monitor each state variable and total disturbance in real time based on system control quantity and output [17]. The output errors of LTD and LESO, combined with total disturbance observations after LESF operation, form the system control quantity. As a result, the controlled object is simplified into a series integrator form.

4.2. Design of Torque ADRC Controller

The mechanical motion equation of the rotor is:

$$T_e = J\frac{d\omega}{dt} + D\omega + T_L \tag{11}$$

where T_e is the electromagnetic torque, J the moment of inertia, D the viscous friction coefficient, and T_L the load torque.

Convert to total disturbance form:

$$\dot{\omega} = b_T u + f \tag{12}$$

In the formula, $b_T = 1/J$, $u = T_e$, total disturbance $f = (D\omega + T_L)/J$, state variable $x_1 = \omega$, extended state variable $x_2 = f$. Convert to state space equation form:

$$\begin{cases} \dot{\mathbf{x}} = \mathbf{A}\mathbf{x} + \mathbf{B}\mathbf{u} + \mathbf{E}h \\ \mathbf{y} = \mathbf{C}\mathbf{x} \end{cases} \tag{13}$$

In the equation, the state matrix and total perturbation differential term are shown in Equation (14):

$$\begin{cases} \mathbf{x} = \begin{bmatrix} x_1 & x_2 \end{bmatrix}^\top \\ \mathbf{A} = \begin{bmatrix} 0 & 1 \\ 0 & 0 \end{bmatrix} \\ \mathbf{B} = \begin{bmatrix} b_T & 0 \end{bmatrix}^\top \\ \mathbf{C} = \begin{bmatrix} 1 & 0 \end{bmatrix} \\ \mathbf{E} = \begin{bmatrix} 0 & 1 \end{bmatrix}^\top \\ h = \dot{f} \end{cases} \tag{14}$$

The torque ADRC controller is designed according to the above formula, where the first-order tracking differentiator is:

$$\begin{cases} e_1 = \omega_1 - \omega_{ref} \\ \dot{\omega}_1 = -re_1 \end{cases} \tag{15}$$

The second order extended state observer is:

$$\begin{cases} e_2 = z_1 - \omega \\ \dot{z}_1 = z_2 - \beta_1 e_2 + bu \\ \dot{z}_2 = -\beta_2 e_2 \end{cases} \tag{16}$$

The linear state error feedback control law is:

$$\begin{cases} e = \omega_1 - z_1 \\ u_0 = ke \\ u = u_0 - z_2/b \end{cases} \tag{17}$$

where ω_1 is the tracking value output by the first-order linear tracking differentiator; ω_{ref} is the given speed of the motor; r is the tracking factor; ω is the actual speed of the motor; z_1 and z_2 are respectively the observed value of the actual speed of the motor and the total disturbance during operation; and β_1 and β_2 are the error gain of the second-order extended state observer. k is the gain of the linear state error feedback control law.

4.3. Design of Suspension Force ADRC Controller

As shown in Figure 11, the bias current of the suspension part is set to 4 A. The mathematical model of the suspension force can be derived again according to the Maxwell stress method.

$$\begin{cases} F = \tilde{k}_i i_c + \tilde{k}_x x_0 \\ \tilde{k}_i = \frac{4\mu_0 SN^2}{g^2} \\ \tilde{k}_x = -\frac{16\mu_0 SN^2}{g^3} \end{cases} \tag{18}$$

Considering the disturbance caused by the rotor suspension process, it can be obtained:

$$F = \tilde{k}_i i_c + \tilde{k}_x x_0 = m\ddot{x} + d \tag{19}$$

Convert to total disturbance form:

$$\ddot{x} = b_F u + \tilde{f} \tag{20}$$

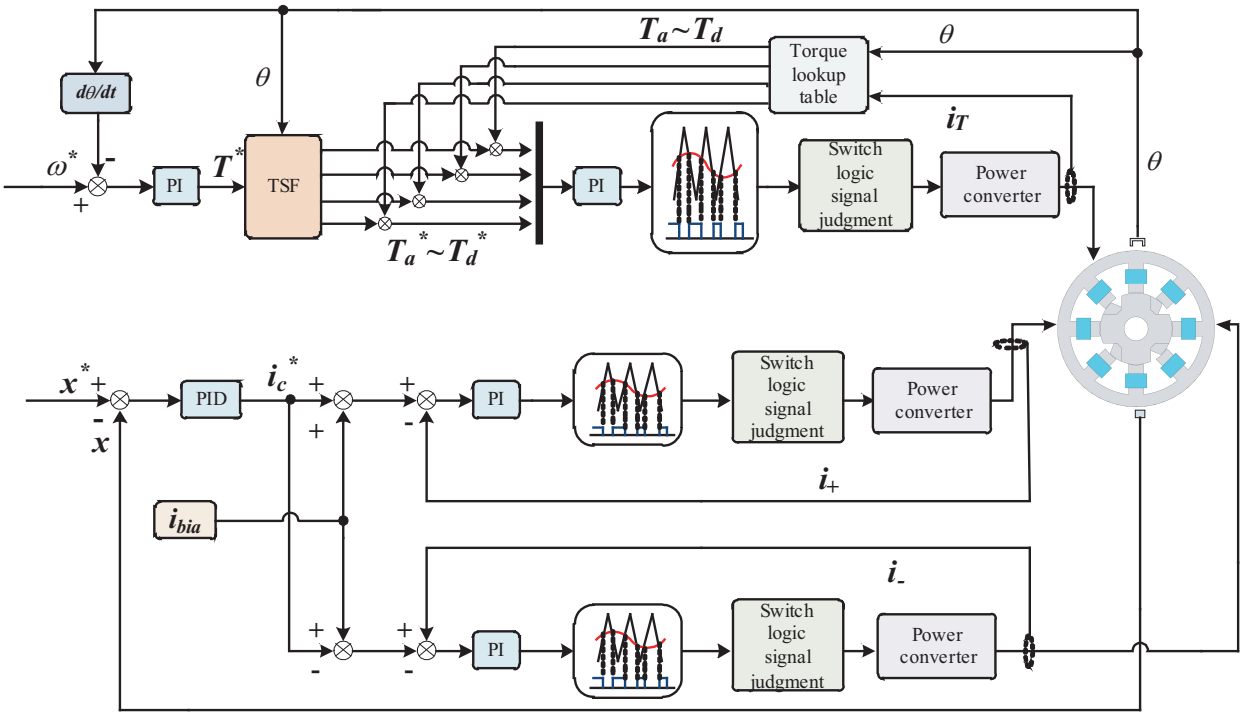

FIGURE 13. The three-unit 8/4 wide-rotor BSRM control system.

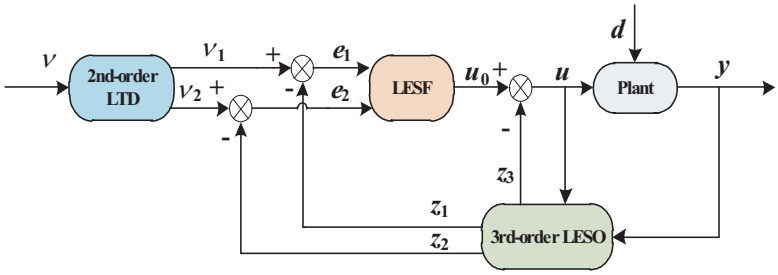

FIGURE 14. Active disturbance rejection controller.

In the equation, $b_F = \tilde{k}_i/m$, $u = i_c$, total disturbance $f = (k_x x_0 - d)/m$, state variables x_1 and x_2 are respectively rotor displacement and velocity. Expanded state variable x_3 is the total disturbance, and Equation (20) is converted into the form of state-space equation:

$$\begin{cases} \dot{\mathbf{x}} = \tilde{\mathbf{A}}\mathbf{x} + \tilde{\mathbf{B}}\mathbf{u} + \tilde{\mathbf{E}}\tilde{h} \\ \mathbf{y} = \tilde{\mathbf{C}}\mathbf{x} \end{cases} \tag{21}$$

The state matrix and total perturbation differential term are shown in Equation (22):

$$\begin{cases} \mathbf{x} = \begin{bmatrix} x_1 & x_2 & x_3 \end{bmatrix}^\top \\ \tilde{\mathbf{A}} = \begin{bmatrix} 0 & 1 & 0 \\ 0 & 0 & 1 \\ 0 & 0 & 0 \end{bmatrix} \\ \tilde{\mathbf{B}} = \begin{bmatrix} 0 & b_F & 0 \end{bmatrix}^\top \\ \tilde{\mathbf{C}} = \begin{bmatrix} 1 & 0 & 0 \\ 0 & 1 & 0 \\ 0 & 0 & 1 \end{bmatrix} \\ \tilde{\mathbf{E}} = \begin{bmatrix} 0 & 0 & 1 \end{bmatrix}^\top \\ \tilde{h} = \dot{f} \end{cases} \tag{22}$$

The displacement control objective is that the rotor is stably suspended in the equilibrium position. The reference input is the rotor eccentricity distance 0, which is a constant signal, and its differential is also a constant signal, so there is no need for the LTD module to generate the transition process and differential signal of the reference input. The third-order extended state observer is:

$$\begin{cases} e = z_1 - y \\ \dot{z}_1 = z_2 - l_1 e \\ \dot{z}_2 = z_3 - l_2 e + bu \\ \dot{z}_3 = -l_3 e \end{cases} \tag{23}$$

The linear error feedback control law is:

$$\begin{cases} e_1 = v_1 - z_1 \\ e_2 = v_2 - z_2 \\ u_0 = k_1 e_1 + k_2 e_2 \\ u = u_0 - z_3/b \end{cases} \tag{24}$$

where v_1 is the reference input signal, and v_2 is the differential signal of the reference input. l_1, l_2, l_3 are the error gain of

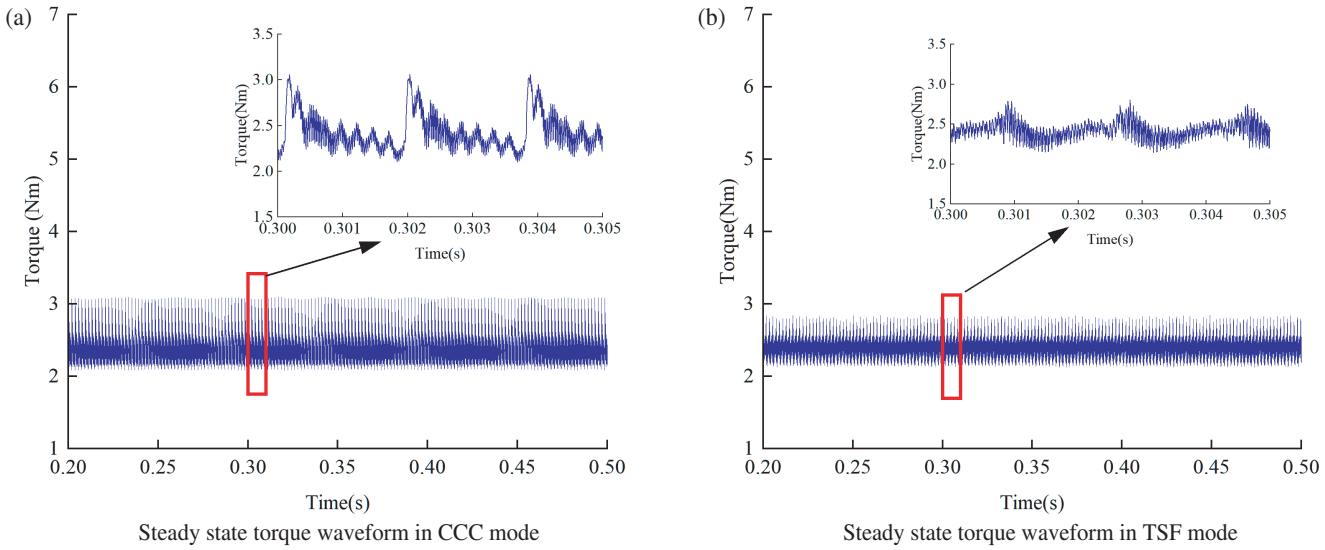

Steady state torque waveform in CCC mode

Steady state torque waveform in TSF mode

FIGURE 15. Steady state torque under CCC and TSF control.

TABLE 2. Three-unit 8/4 wide-rotor BSRM simulation parameters.

Argument	value	Argument	value
Rotor inner diameter/mm	20	Stator pole arc/deg	24
Rotor yoke thickness/mm	10	Number of turns	37
Rotor tooth length/mm	10	Motor unit 1 length/mm	27.5
Air gap length/mm	0.5	Motor unit 2 length/mm	27.5
Stator tooth length/mm	25	Motor unit 3 length/mm	55
Stator yoke thickness/mm	10	Rotor mass/kg	5
Rotor pole arc/deg	48	DC voltage/V	220

the third-order extended state observer, and k_1, k_2 are the gain coefficients of the linear error feedback control law.

4.4. Parameter Tuning

According to the design process of the ADRC controller above, five parameters of the speed controller, including tracking factor r, second-order LESO error gain β_1 and β_2, control quantity gain b_T, and LSEF error gain k, need to be adjusted. In the displacement controller, six parameters of third-order LESO error gain l_1, l_2, l_3, control gain b_F, and LSEF error gain k_1, k_2 need to be adjusted. Among them, b_T and b_F can be calculated by the structural parameters of the motor, so only the remaining 9 parameters need to be adjusted.

The larger the tracking factor r is, the faster the tracking speed of the reference signal will be, but it should not be too large; otherwise it will cause the tracking signal to oscillate [16]. According to [11], in order to ensure system stability and simplify parameter adjustment, the poles of LESO and LSEF are assigned at $-\omega_o$ and $-\omega_c$ on the left half real axis of the complex plane, respectively. The specific configurations are as follows:

$$\begin{cases} \beta_1 = 2\omega_{To} \\ \beta_2 = \omega_{To}^2 \\ k = \omega_{Tc} \end{cases} \tag{25}$$

where ω_{To} and ω_{Tc} are the observer bandwidth and controller bandwidth of the torque ADRC controller respectively.

$$\begin{cases} l_1 = 3\omega_{Fo} \\ l_2 = 3\omega_{Fo}^2 \\ l_3 = \omega_{Fo}^3 \\ k_1 = \omega_{Fc}^2 \\ k_2 = 2\omega_{Fc} \end{cases} \tag{26}$$

In Equations (25) and (26), ω_{Fo} and ω_{Fc} are the observer bandwidth and controller bandwidth of the suspension force ADRC controller, respectively.

5. SIMULATION RESULTS

The simulation parameters of the three-unit 8/4 wide-rotor BSRM are shown in Table 2.

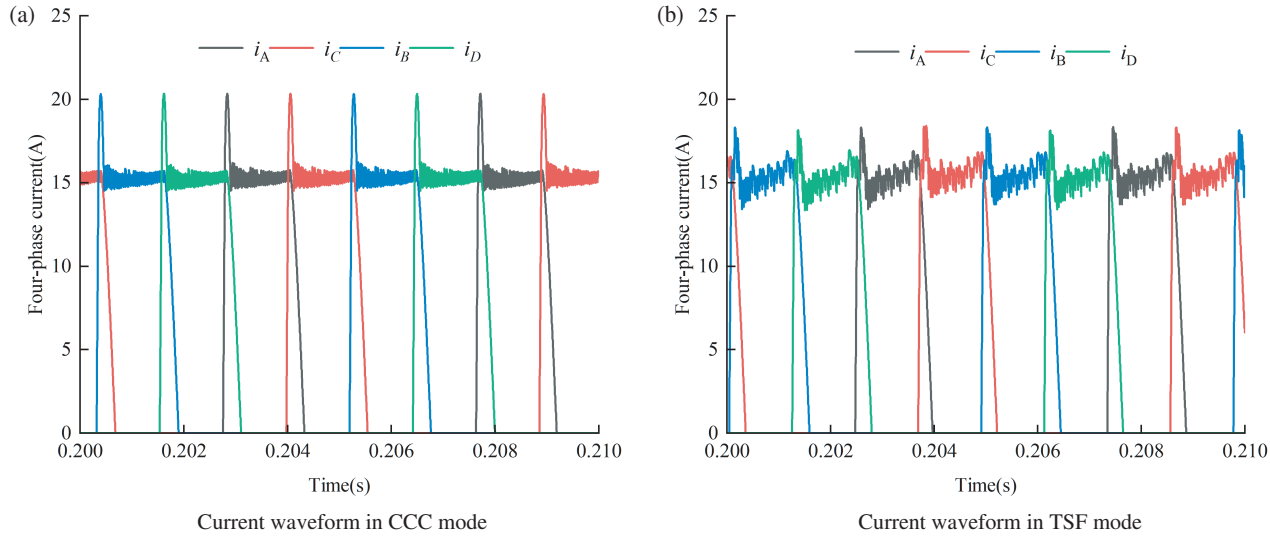

FIGURE 16. Current under CCC and TSF control.

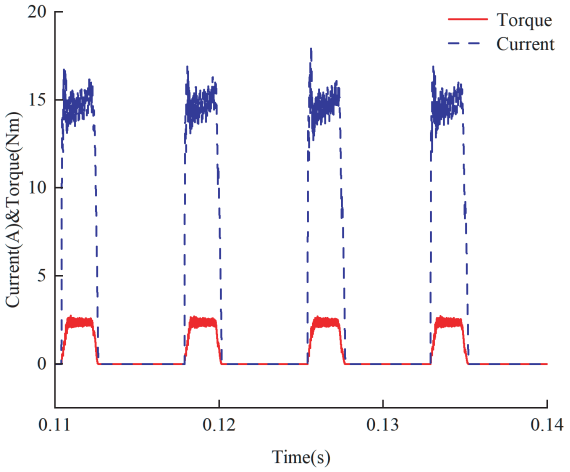

FIGURE 17. Phase torque and phase current relationship.

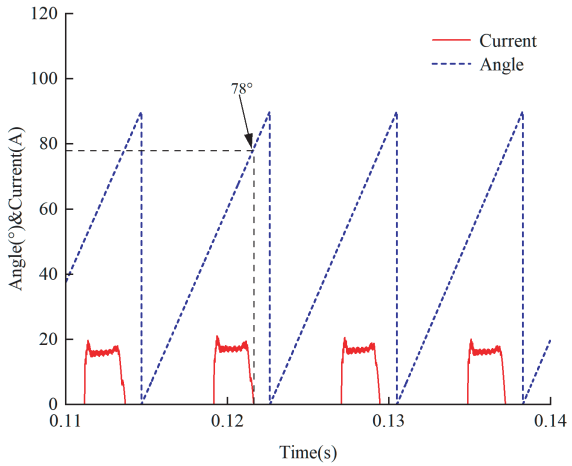

FIGURE 18. Rotor position Angle and winding current relationship.

Current chopper control (CCC) is a traditional torque control strategy. Given a speed of 3000 r/min and load torque of 2 Nm, the torque ripple suppression effects of CCC and TSF control strategies are compared. Define the torque ripple coefficient:

$$T_{rip} = \frac{T_{\max} - T_{\min}}{T_{ave}} \times 100\% \tag{27}$$

where $T_{\max}$, $T_{\min}$, and T_{ave} are the maximum, minimum, and average values of torque, respectively.

Figure 15 shows that under the same working conditions, the torque ripple suppression effect of TSF control strategy is significantly better than that of the traditional CCC control strategy. The torque ripple coefficient is quantitatively calculated, and $T_{rip} = 41.2\%$ under CCC mode, while $T_{rip} = 29.6\%$ under TSF mode, a relative reduction of 28.2%.

Figure 16 shows the torque current waveform under the two control modes. The turn-on angle of SRM is generally set in the lower flat top area of the inductor, and the inductance change rate is low. In the traditional CCC mode, only the current is controlled, but when the rotor is rotated to the turn-on angle, a large current is needed to quickly track the given torque, so there is a certain current spike, which increases the operating loss. However, in the TSF mode, the given torque of the excitation phase rises according to the sine law, and a small current can track the given torque, so the current peak is smaller, and the operating loss is relatively lower.

To solve the problem of weak coupling of torque current to suspension force, the end point of commutation overlap area is set at the maximum inductance value. Taking phase A as an example, the simulation results according to this scheme are shown in Figure 17 and Figure 18.

Figure 17 shows that the phase torque drops to 0 at the same time as the phase current. The analysis shows that the linear model of the torque of the switched reluctance motor is as follows:

$$T_e = \frac{1}{2} \cdot \frac{dL}{d\theta} \cdot i^2 \tag{28}$$

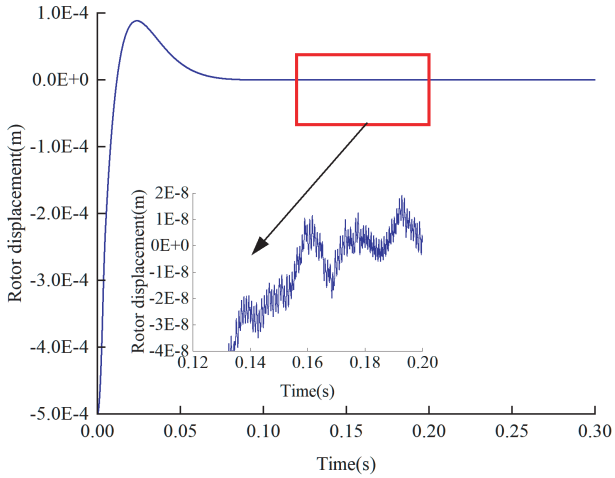

FIGURE 19. Rotor lifting displacement waveform under suspension current PWM strategy.

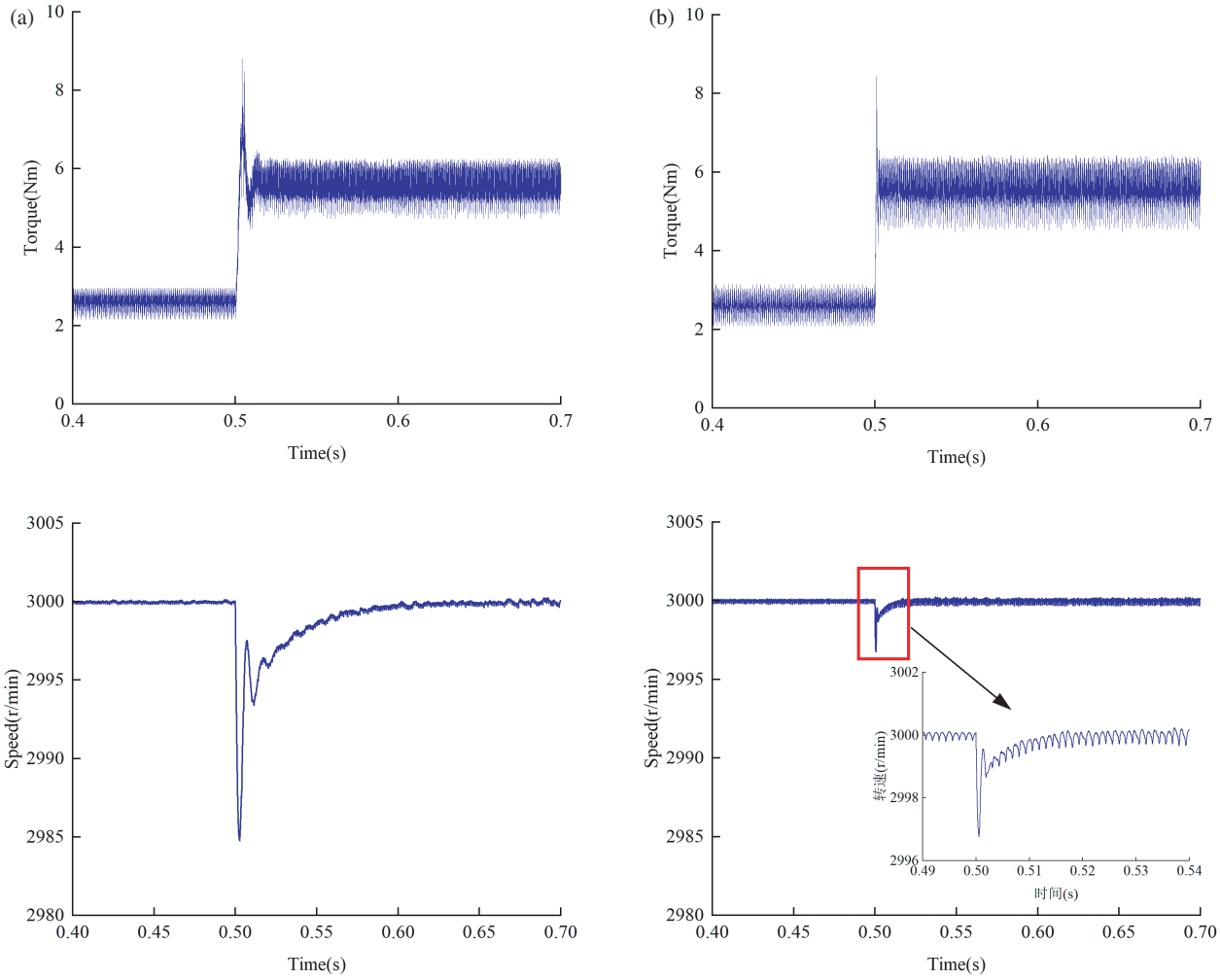

PID control torque and speed waveform under sudden load disturbance

ADRC controls torque and speed waveform under sudden load disturbance

FIGURE 20. Comparison of speed under sudden load disturbance.

When phase A ends single-phase conduction and enters the commutation overlap area, the given torque of phase A begins to decline according to the sine law. Before reaching the maximum inductance, the inductance change rate is not 0, so under the action of PWM modulation, the torque current decreases un-

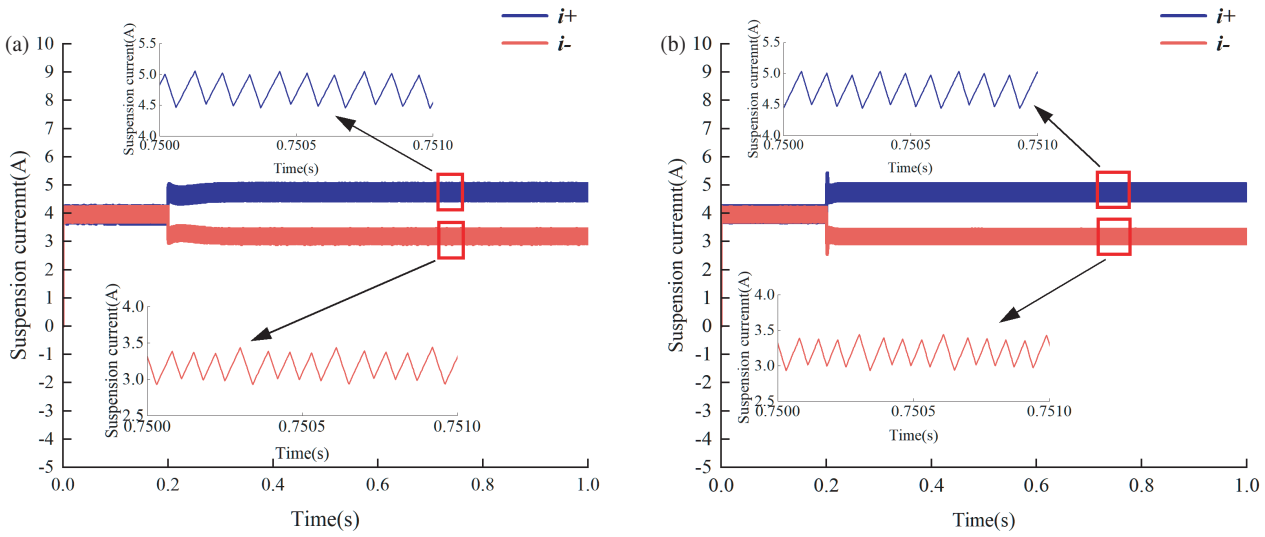

FIGURE 21. The suspension current under different controllers with sudden radial disturbance.

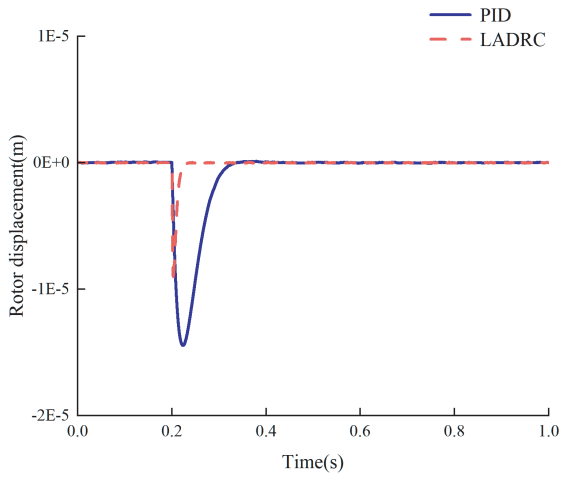

FIGURE 22. Comparison of rotor displacement under different controllers with abrupt radial disturbance.

til the maximum inductance is reached. At this time, the given torque decreases to 0.

The position at which the rotor tooth pole axis is aligned is 0°. According to Table 2 and Figure 18, it can be seen that the torque current of phase A is exactly at the rotor position Angle of 78°, that is, the inductance maximum value drops to 0. After switching to the suspended phase, the suspension force is completely generated by the control current of the radial relative winding and has nothing to do with the continuity of the torque current. In order to verify the effectiveness of rotor lifting and suspension current PWM strategy, the suspension force control system is rebuilt according to Equation (19), and the simulation results are shown in Figure 19.

In Figure 19, simulation results show that the suspension current PWM control can make the rotor float stably, with a maximum displacement of 8×1^{-5} m, and return to the equilibrium state after about 0.16 s. During stable operation, there is a fluctuation of 4×10^{-8} m, with good suspension accuracy, which verifies the correctness of the mathematical model and the suppression effect of the suspension force pulsation of the adopted control strategy.

The design of the above control system is based on the traditional PID controller, and the suppression effect of the external disturbance is limited. Therefore, the ADRC controller is used to replace the traditional PID controller, and the simulation is compared under the same working conditions. The suppression abilities of traditional PID controller and LADRC controller for sudden load disturbance and radial external force disturbance are compared and analyzed in terms of torque and suspension.

The load torque at 0.5 s changes sharply from 2 Nm to 5 Nm. In Figure 20, the simulation results show that PID controller is used to restore steady state at 0.6 s, and the speed decreases by 15 r/min, while LADRC controller is used to restore steady state at 0.52 s; the speed decreases by 3 r/min; the response time is relatively increased by 80%; and the speed decline is relatively reduced by 80%. Therefore, in the torque control system, compared with the traditional PID controller, LADRC controller has a stronger ability to suppress external interference.

As shown in Figure 21 and Figure 22, when external force is applied abruptly in the radial direction, the variation law of the suspension current of the radial relative winding of different controllers is consistent, and the control current and bias current are superimposed and offset each other to perform asymmetric excitation of the winding. PID controller is used to restore steady state at 0.4 s, and the maximum rotor displacement is 1.5×10^{-5} m. LADRC controller is used to restore steady state at 0.24 s; the maximum rotor displacement is 1×10^{-5} m; the response time is reduced by 80%; and the maximum rotor displacement is 33.3% lower. Therefore, in the suspension control system, compared with the traditional PID controller, the LADRC controller has a stronger ability to suppress the external interference.

6. CONCLUSION

In this paper, a novel three-unit 8/4 wide-rotor BSRM is proposed. Its unique body structure significantly reduces the coupling of torque and suspension force. Additionally, to address the torque ripple and suspension force pulsation caused by the switching power supply and double salient pole structure of the motor, a torque sharing function and suspension current PWM control strategy are employed to suppress the pulsations. The torque sharing function is utilized to resolve the weak coupling problem between torque current and current stiffness coefficient as well as displacement stiffness coefficient when each phase switches from torque phase to suspension phase. Furthermore, in order to enhance the anti-disturbance performance of the motor, an ADRC controller is introduced to demonstrate its superiority in disturbance suppression compared with traditional PID controller. However, the suspension force control system in this paper only aims to suppress the suspension force ripple, but according to the inductance curve of the three-element 8/4 wide rotor BSRM, the inductance enters the descent zone immediately after the end of the upper flat top zone, and if there is still current in the winding at this time, negative torque will be generated and the torque ripple increased. Therefore, based on the suspension current PWM control system, it is planned to further analyze the variation law of the suspension force during the two-phase exchange operation, so as to suppress the suspension force pulsation and avoid the negative torque.

ACKNOWLEDGEMENT

Y. H. Huang acknowledges National Natural Science Foundation of China (NSFC) (Contract 52377053).

REFERENCES

[1] Takemoto, M., H. Suzuki, A. Chiba, T. Fukao, and M. A. Rahman, "Improved analysis of a bearingless switched reluctance motor," *IEEE Transactions on Industry Applications*, Vol. 37, No. 1, 26–34, 2001.

[2] Oshima, M., S. Miyazawa, T. Deido, A. Chiba, F. Nakamura, and T. Fukao, "Characteristics of a permanent magnet type bearingless motor," *IEEE Transactions on Industry Applications*, Vol. 32, No. 2, 363–370, 1996.

[3] Yuan, Y., Y. Sun, and Y. Huang, "Radial force dynamic current compensation method of single winding bearingless flywheel motor," *IET Power Electronics*, Vol. 8, No. 7, 1224–1229, 2015.

[4] Zhu, J., Z. Deng, X. Wang, and Q. X. Liao, "Principle and implementation of the single winding bearingless permanent magnetic slice motor," *Proceedings of the CSEE*, Vol. 28, No. 33, 68–74, 2008.

[5] Yan, N., X. Cao, L. Zhang, *et al.*, "Direct torque control-based model predictive control of switched reluctance motors," *Proceedings of the CSEE*, Vol. 37, No. 18, 5446–5453, 2017.

[6] Morrison, C. R., M. W. Siebert, and E. J. Ho, "Electromagnetic forces in a hybrid magnetic-bearing switched-reluctance motor," *IEEE Transactions on Magnetics*, Vol. 44, No. 12, 4626–4638, 2008.

[7] Yang, G., Z. Deng, X. Cao, *et al.*, "Control strategy of average levitated force of a bearingless switched reluctance motor," *Acta Aeronautica ET Astronautica Sinica*, Vol. 30, No. 3, 505–511, 2009.

[8] Sun, J., Q. Zhan, and L. Liu, "Modelling and control of bearingless switched reluctance motor based on artificial neural network," in *31st Annual Conference of IEEE Industrial Electronics Society, 2005. IECON 2005.*, 1638–1643, Raleigh, NC, USA, 2005.

[9] Hao, Z., X. Cao, X. Deng, and X. Shen, "Novel bearingless switched reluctance motor with wide flat inductance region to simplify the control of torque and levitation force," *IEEE Transactions on Energy Conversion*, Vol. 35, No. 3, 1278–1288, 2020.

[10] Han, J., *Self-disturbance Control Technology*, National Defense Industry Press, Beijing, 2008.

[11] Gao, Z., "Scaling and bandwidth-parameterization based controller tuning," in *American Control Conference*, 4989–4996, 2003.

[12] Cao, X., C. Liu, Z. Deng, *et al.*, "Decoupling mechanism and realization of torque and suspension force of single-winding 12/4 pole bearingless switched reluctance motor," *Transactions of China Electrotechnical Society*, Vol. 33, No. 15, 3527–3534, 2018.

[13] Yuan, Y., T. Shi, Y. Sun, *et al.*, "Decoupling control of suspension system for 12/14 bearingless switched reluctance motor," *Proceedings of the CSEE*, Vol. 43, No. 23, 9310–9319, 2023.

[14] Cheng, Y., X.-X. Cao, and Y.-L. Zhang, "Hysteresis-PWM direct instantaneous torque control of switched reluctance motor," *Electric Machines & Control*, Vol. 24, No. 8, 74–82, 2020.

[15] Hu, Y., Z. Kang, D. Sun, *et al.*, "Torque ripple suppression of switched reluctance motor based on interval segmentation torque sharing function," *Electric Machines and Control*, Vol. 27, No. 10, 54–62, 2023.

[16] Xia, L., T. Sun, X. Li, *et al.*, "Research on servo control system based on linear active disturbance rejection control technology," *Journal of Electrical Engineering*, Vol. 8, No. 04, 3–49, 2023.

[17] Meng, J., X. Wu, Z. Zhang, *et al.*, "Adaptive linear active disturbance rejection control method and ripple suppression compensation strategy for three-phase isolated AC-DC-DC power supply," *Transactions of China Electrotechnical Society*, Vol. 38, No. 14, 3898–3908, 2023.